Supplemental Material for "Anderson Delocalization in Strongly-Coupled Disordered Non-Hermitian Chains"

Wei-Wu Jin,[1,*] Jin Liu,[1,*] Xin Wang,[2] Yu-Ran Zhang,[1] Xue-Qin Huang,[1]
Xiaomin Wei,[1] Wenbo Ju,[1,†] Zhongmin Yang,[1,3,4,‡] Tao Liu,[1,§] and Franco Nori[5,6]

[1]School of Physics and Optoelectronics, South China University of Technology, Guangzhou 510640, China
[2]Institute of Theoretical Physics, School of Physics, Xi'an Jiaotong University, Xi'an 710049, China
[3]Research Institute of Future Technology, South China Normal University, Guangzhou 510006, China
[4]State Key Laboratory of Luminescent Materials and Devices and Institute of Optical Communication Materials, South China University of Technology, Guangzhou 510640, China
[5]Center for Quantum Computing, RIKEN, Wakoshi, Saitama 351-0198, Japan
[6]Department of Physics, University of Michigan, Ann Arbor, Michigan 48109-1040, USA

(Dated: July 24, 2025)

I. PHYSICAL MECHANISM

To gain intuitive insight into the physical mechanism behind Anderson delocalization accompanied by the re-emergence of the non-Hermitian skin effect (NHSE) under anti-symmetrically correlated disorder, we consider the regime of strong inter-chain coupling. Specifically, we assume $|t| \gg |J|, |\gamma \pm \lambda|, |\Delta_j|$, for both symmetric and anti-symmetric disorder configurations. In this limit, inter-chain hopping dominates the dynamics, allowing us to treat the intra-chain hopping terms as perturbations. The Hamiltonian $\hat{\mathcal{H}}$ is thus decomposed as $\hat{\mathcal{H}}_{\pm} = \hat{\mathcal{H}}_{0,\pm} + \hat{\mathcal{V}}$, with the unperturbed part reading

$$\hat{\mathcal{H}}_{0,\pm} = \sum_j \left[t\left(a_j^\dagger \hat{b}_j + \text{H.c.}\right) + \Delta_j \left(a_j^\dagger a_j \pm \hat{b}_j^\dagger \hat{b}_j\right)\right], \tag{S1}$$

and the perturbed part as

$$\hat{\mathcal{V}} = \sum_j \left[(\gamma+\lambda)\hat{a}_j^\dagger \hat{a}_{j+1} + (\gamma-\lambda)\hat{a}_{j+1}^\dagger \hat{a}_j\right] + \sum_j J\left(\hat{b}_{j+1}^\dagger \hat{b}_j + \text{H.c.}\right), \tag{S2}$$

where $\hat{\mathcal{H}}_+$ denotes the coupled chains under the symmetric disorder configuration, and $\hat{\mathcal{H}}_-$ under the anti-symmetric disorder configuration.

In the strong inter-chain coupling limit, with $|t| \gg |J|, |\gamma \pm \lambda|, |\Delta_j|$, $\mathcal{H}_{0,\pm}$ can be rewritten as

$$\hat{\mathcal{H}}_{0,\pm} = \sum_{j,m=\pm} \xi_{\pm,j}^{(m)} \hat{\alpha}_{m,j}^\dagger \hat{\alpha}_{m,j}, \tag{S3}$$

where $\hat{\alpha}_{\pm,j}$ and $\xi_{\pm,j}^{\pm}$ are

$$\hat{\alpha}_{\pm,j} = (\pm\hat{a}_j + \hat{b}_j)/\sqrt{2}, \tag{S4}$$

$$\xi_{+,j}^{\pm} = \Delta_j \pm t, \quad \text{and} \quad \xi_{-,j}^{\pm} = \pm\sqrt{t^2 + \Delta_j^2}. \tag{S5}$$

In the new basis $|\alpha_\pm, j\rangle = \hat{\alpha}_{\pm,j}^\dagger |0\rangle$, we write $\hat{\mathcal{H}}_\pm$ as $\hat{\tilde{\mathcal{H}}}_\pm = \hat{\mathcal{H}}_{0,\pm} + \hat{\mathcal{H}}_{\text{ladder}}$, with

$$\begin{aligned}\hat{\mathcal{H}}_{\text{ladder}} = {} & \frac{J+\gamma+\lambda}{2}\sum_j \left(\hat{\alpha}_{+,j}^\dagger \hat{\alpha}_{+,j+1} + \alpha_{-,j}^\dagger \hat{\alpha}_{-,j+1}\right) + \frac{J+\gamma-\lambda}{2}\sum_j \left(\hat{\alpha}_{+,j+1}^\dagger \alpha_{+,j} + \hat{\alpha}_{-,j+1}^\dagger \hat{\alpha}_{-,j}\right) \\ & + \frac{J-\gamma-\lambda}{2}\sum_j \left(\hat{\alpha}_{-,j}^\dagger \hat{\alpha}_{+,j+1} + \hat{\alpha}_{+,j}^\dagger \hat{\alpha}_{-,j+1}\right) + \frac{J-\gamma+\lambda}{2}\sum_j \left(\alpha_{+,j+1}^\dagger \hat{\alpha}_{-,j} + \hat{\alpha}_{-,j+1}^\dagger \hat{\alpha}_{+,j}\right).\end{aligned} \tag{S6}$$

In Eq. (S6), we have neglected disorder in the hopping terms, which is quite small for $|\Delta_j| \gg |J|, |\gamma \pm \lambda|$.

In this new basis, the Hamiltonian $\hat{\tilde{\mathcal{H}}}\pm$ takes the form of a nonreciprocal Creutz ladder, denoted $\hat{\mathcal{H}}_{\text{ladder}}$[1], subject to a disordered onsite potential $\hat{\mathcal{H}}0, \pm$. The disorder configuration depends on the symmetry of correlations: $\hat{\mathcal{H}}_{0,+}$ for symmetric and $\hat{\mathcal{H}}_{0,-}$ for anti-symmetric disorder. For the parameter regime considered in the main text, $\hat{\mathcal{H}}_{\text{ladder}}$ exhibits the non-Hermitian skin effect (NHSE), with all eigenmodes accumulating at the left boundary. In the symmetric disorder case, the effective onsite potential on each chain of the Creutz ladder is given by $\Delta_j \pm t$ ($\Delta_j \in [-W/2,\ W/2]$ denotes random disorder). This disorder leads to the Anderson localization when the disorder strength W becomes sufficiently large.

However, in the case of anti-symmetric disorder, the onsite random potential in each leg of the ladder takes the form $\pm\sqrt{t^2 + \Delta_j^2}$ ($\Delta_j \in [-W/2,\ W/2]$ denotes random disorder). Under this configuration, the effective disorder strength $\tilde{W}$ in the Creutz ladder is bounded as $\tilde{W} < W^2/|8t|$. In the strong inter-chain coupling limit, where $|t| \gg |\Delta_j|$ (i.e., $|t| \gg W$), this results in a disorder strength $\tilde{W}$ that is significantly weaker than the nonreciprocal hopping amplitude λ. While even infinitesimal disorder induces Anderson localization in one-dimensional Hermitian systems[2], it has been shown that the interplay between nonreciprocal hopping and disorder can instead lead to an Anderson transition[3,4]. Consequently, as the inter-chain hopping t increases, the NHSE can re-emerge, even in the presence of arbitrarily strong disorder, provided the disorder remains anti-symmetric.

II. EIGENENERGY-RESOLVED IPR AND mcom

In the main text, we utilize the IPR and mcom, averaged over all eigenstates and disorder realizations, to distinguish between skin-mode localization and Anderson localization. By averaging over the full spectrum, we capture the collective localization behavior of the system. Although the eigenstate ensemble may contain both localized and extended states, the averaged IPR reflects the system's overall tendency toward localization or delocalization. In combination with the IPR, the averaged mcom serves as an effective diagnostic tool for identifying skin-mode localization, characterized by mcom ~ 1 or mcom $\sim N$, and for distinguishing it from Anderson localization, which typically yields mcom $\sim N/2$. Without this distinction, the two types of localization—skin-mode and Anderson—would be mixed.

In this section, we present eigenenergy-resolved results for IPR_n and mcom_n, averaged over disorder realizations. These results demonstrate that IPR and mcom, averaged over all eigenstates and disorder realizations, can indeed be effectively employed to detect localization and to distinguish between skin-mode and Anderson localization in the system.

Each skin mode can be identified by evaluating the eigenenergy-resolved mean center of mass mcom_n, which quantifies the spatial localization of the squared amplitude of each eigenstate, averaged over disorder realizations. The eigenenergy-resolved mcom is defined as

$$\text{mcom}_n = \frac{\sum_{j=1}^{N} j \, \langle \mathcal{A}_n(j) \rangle}{\sum_{j=1}^{N} \langle \mathcal{A}_n(j) \rangle}, \tag{S7}$$

with $\langle \mathcal{A}_n(j) \rangle$ being

$$\langle \mathcal{A}_n(j) \rangle = \left\langle \left(|\psi_n^{(a)}(j)|^2 + |\psi_n^{(b)}(j)|^2 \right) \right\rangle, \tag{S8}$$

where $\langle \cdot \rangle$ indicates disorder averaging. When mcom_n is close to 1 or N, it indicates that the eigenstate is localized at the boundaries, signaling the emergence of the NHSE. In contrast, Anderson localization typically yields mcom $\sim N/2$, reflecting bulk localization.

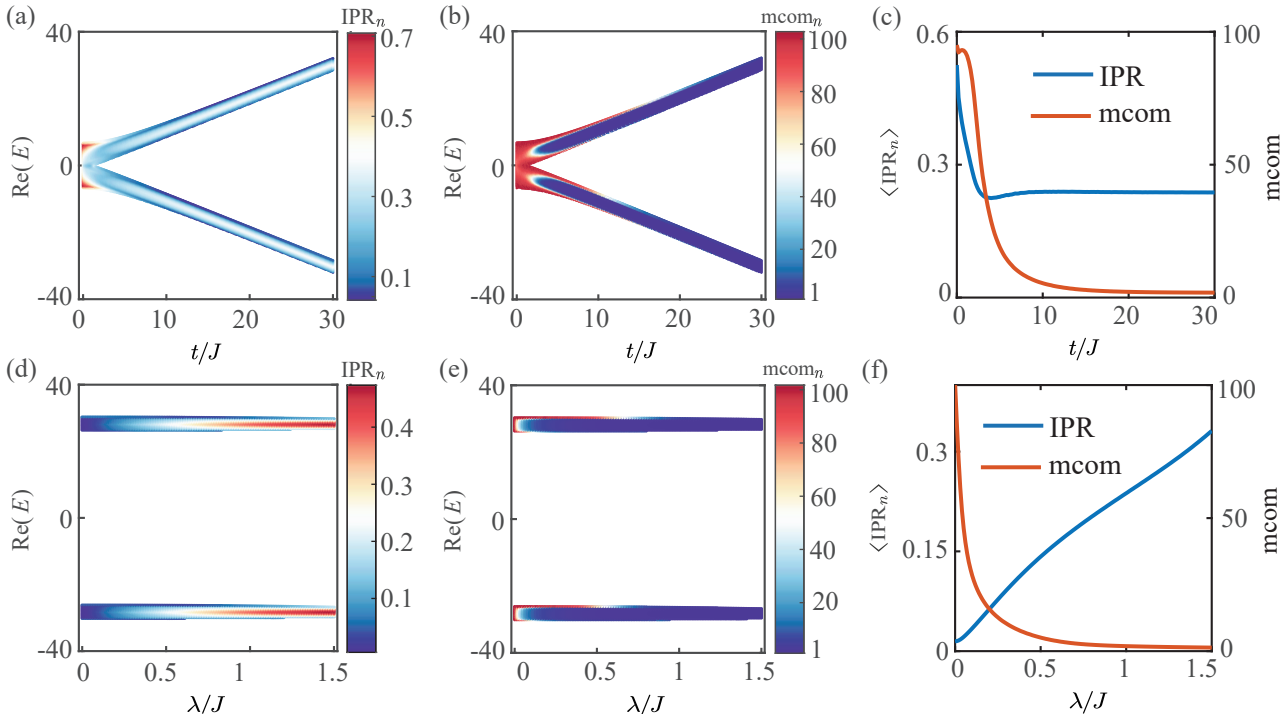

FIG. S1. Eigenenergy-resolved IPR$_n$ and mcom$_n$ of the coupled chain, subject to anti-symmetrically correlated disorder with $\Delta_j^{(a)} = -\Delta_j^{(b)} = \Delta_j$, plotted as a function of coupling strength t for $W/J = 12$ and $\lambda/J = 1$ (a,b), and as a function of asymmetric hopping strength λ for $W/J = 12$ and $t/J = 28$ (d,e). The corresponding IPR averaged over all the eigenstates are shown in (c,f). The remaining parameters are fixed at $\gamma/J = 1$ and $N = 200$. All results are averaged over 2000 disorder realizations.

Figure S1 shows the eigenenergy-resolved IPR$_n$ of the coupled chain, subject to anti-symmetrically correlated disorder with $\Delta_j^{(a)} = -\Delta_j^{(b)} = \Delta_j$, as functions of the inter-chain hopping strength t in (a) and the asymmetric intra-chain hopping strength λ in (d). The localized and extended states are clearly resolved by the IPR$_n$: a finite value IPR$_n \sim 1/M$ (with $M \ll N$) indicates localization, while IPR$_n \sim 1/(2N)$ corresponds to extended states. These localization features are also reflected in the IPR averaged over all eigenstates and disorder realizations, as shown in Fig. S1(c,f). However, it is important to note that the IPR alone cannot distinguish between skin-mode localization and Anderson localization.

In order to distinguish skin-mode localization from Anderson localization, we calculate the eigenenergy-resolved mcom$_n$ as functions of the inter-chain hopping strength t [see Fig. S1(b)] and the asymmetric intra-chain hopping strength λ [see Fig. S1(e)]. As either t or λ increases, the system undergoes a transition: initially, all eigenstates are Anderson localized, characterized by mcom$_n \sim N/2$. Then, the system enters a regime where skin-mode localization and Anderson localization coexist. Eventually, all states become skin modes with mcom$_n \sim 1$. These distinct regimes are also captured by the mcom averaged over all eigenstates [see Fig. S1(c,f)]: mcom $\sim N/2$ indicates Anderson localization, mcom ~ 1 signals skin-mode localization, and intermediate values reflect the coexistence of both localization types.

III. FINITE-SIZE EFFECTS

In the main text, the Anderson localization-delocalization transition is investigated using a fixed lattice size. In this section, we examine the impact of varying the lattice size N on the localization behavior and demonstrate that

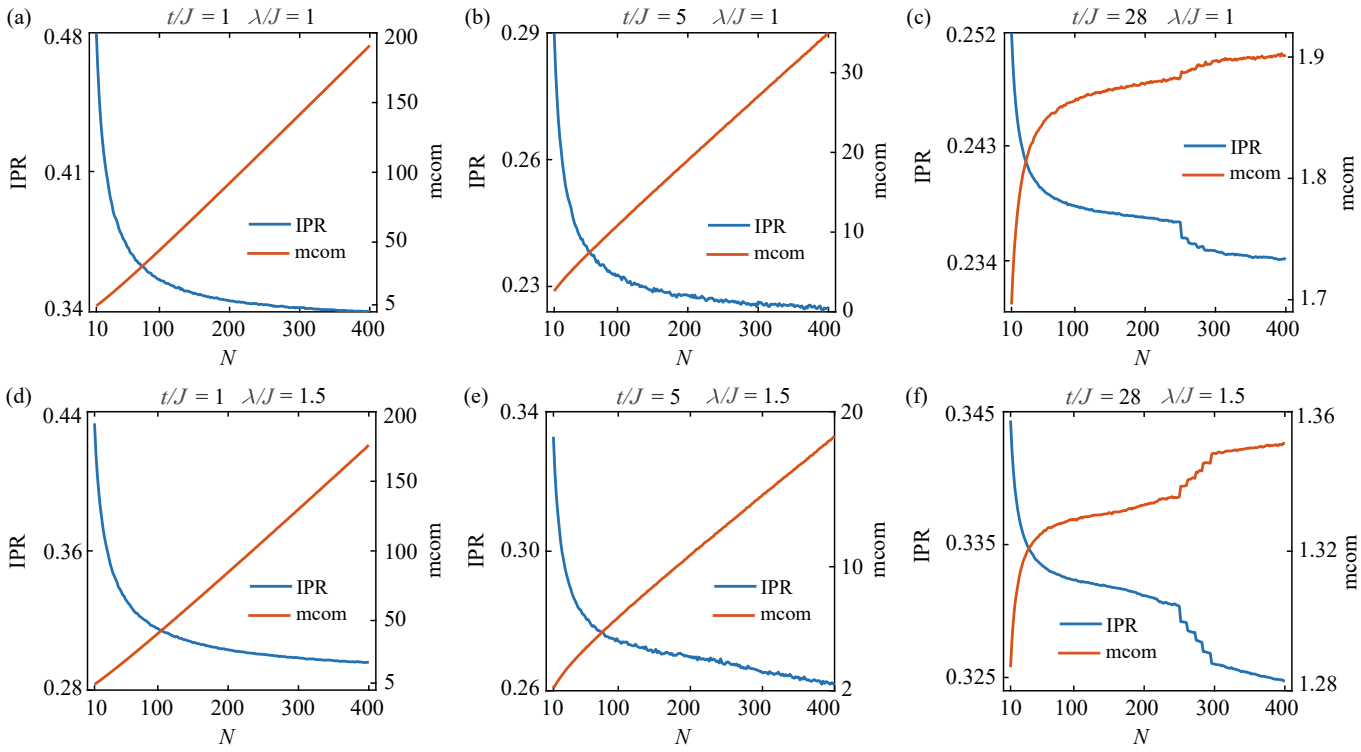

FIG. S2. Impact of lattice size on Anderson localization and delocalization. IPR and mcom averaged over all the eigenstates, subject to anti-symmetric disorder, as a function of lattice size N (a) for $t/J = 1$ and $\lambda/J = 1$, (b) for $t/J = 5$ and $\lambda/J = 1$, (c) for $t/J = 28$ and $\lambda/J = 1$, (d) for $t/J = 1$ and $\lambda/J = 1.5$, (e) for $t/J = 5$ and $\lambda/J = 1.5$, and (f) for $t/J = 28$ and $\lambda/J = 1.5$. The results are averaged over 1200 disorder realizations with $\gamma/J = 1$ and $W/J = 12$.

the conclusions presented in the main text remain unchanged as the lattice size is further increased.

Figure S2 shows the IPR and mcom, averaged over all eigenstates and subject to anti-symmetric disorder, as functions of the lattice size N for different inter-chain coupling strengths t and asymmetric intra-chain hopping amplitudes λ. For Anderson-localized phases with mcom $\sim N/2$ [see Fig. S2(a,d)] and for skin-mode localization with mcom ~ 1 [see Fig. S2(c,f)], the phase identification remains robust and largely independent of system size. In both cases, the mcom serves as a clear and reliable phase indicator. However, in the coexistence regime of Anderson and skin-mode localization [see Fig. S2(b,e)], the mcom becomes less effective for small system sizes ($N < 100$), as its value remains low and does not distinguish the mixed phase well from pure skin-mode localization. To resolve this phase more clearly, the mcom should be evaluated in larger systems. In contrast, the IPR provides a consistent indicator of localization properties even for a small-size system size.

IV. BIORTHOGONAL INVERSE PARTICIPATION RATIO

In the main text, we use the inverse participation ratio (IPR) based on right eigenstates to characterize localization properties. As an alternative, one can also consider the biorthogonal inverse participation ratio (BIPR)[5], defined as

$$\mathrm{BIPR}_n = \frac{\sum_{j=1}^{N}\left(|\psi_{n,L}^{(a)}(j)|^2|\psi_{n,R}^{(a)}(j)|^2 + |\psi_{n,L}^{(b)}(j)|^2|\psi_{n,R}^{(b)}(j)|^2\right)}{\left(\sum_{j=1}^{N}|\psi_{n,L}^{(a)}(j)||\psi_{n,R}^{(a)}(j)| + |\psi_{n,L}^{(b)}(j)||\psi_{n,R}^{(b)}(j)|\right)^2}, \tag{S9}$$

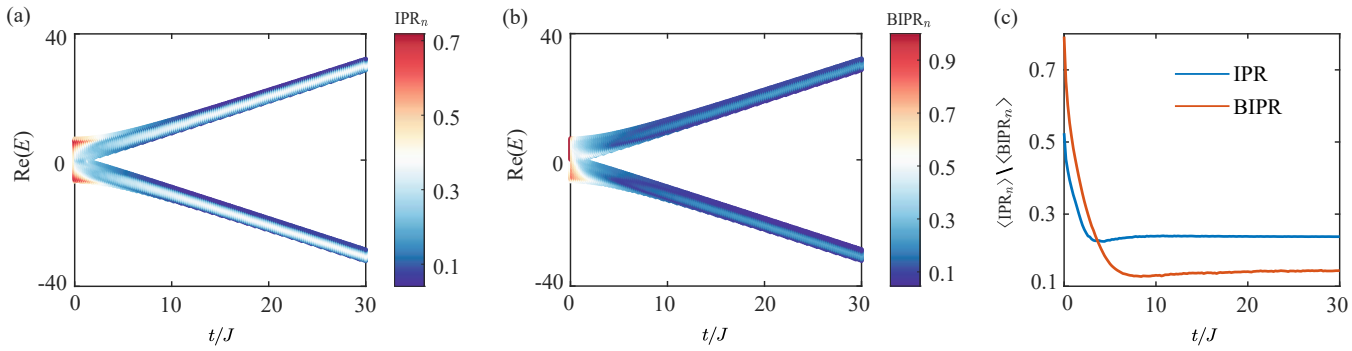

FIG. S3. Eigenenergy-resolved IPR_n (a) and BIPR_n (b) of the coupled chain, subject to anti-symmetrically correlated disorder with $\Delta_j^{(a)} = -\Delta_j^{(b)} = \Delta_j$, plotted as a function of coupling strength t. The corresponding IPR and BIPR averaged over all the eigenstates are shown in (c). The remaining parameters are fixed at $W/J = 12$, $\gamma/J = 1$ and $N = 200$. All results are averaged over 1200 disorder realizations.

where $\psi_{n,L}^{(a)}$ and $\psi_{n,R}^{(a)}$ ($\psi_{n,L}^{(a)}$ and $\psi_{n,R}^{(a)}$) are left and right eigenstates in chain a (b) . Here, $\mathrm{BIPR}_n \simeq 1/(2N)$ for an extended eigenstate ψ_n and vanishes as $N \to \infty$, while for a state localized over $M \ll N$ sites, $\mathrm{BIPR}_n \simeq 1/M$ and remains finite in the thermodynamic limit.

Figure S3 presents the eigenenergy-resolved IPR_n (a) and BIPR_n (b) for the coupled chain under anti-symmetrically correlated disorder, plotted as functions of the coupling strength t. The corresponding IPR and BIPR averaged over all eigenstates are shown in panel (c). While the values of the IPR and BIPR differ slightly, both consistently indicate that the system remains in a localized phase, as evidenced by their finite values. This confirms that either measure can effectively characterize localization. Therefore, using the IPR based on the right eigenstates alone is sufficient to distinguish localized states from extended ones.

V. QUENCHED DYNAMICS

The Anderson delocalization accompanied by re-emergent skin modes induced by anti-symmetric disorder can be further examined through the study of quenched evolution dynamics. The initial state is chosen as a Gaussian wavepacket as $\psi_0(j) = \exp\left[-(j-j_0)^2/2\sigma^2\right]/\mathcal{N}$ centered at the site j_0, where $\mathcal{N}$ is the normalization constant, and σ denotes the wavepacket width. The wavefunction at time τ is obtained by numerically calculating $|\psi(j,\tau)\rangle = \exp(-i\mathcal{H}\tau)\,|\psi_0(j)\rangle$. Figure S4 plots quenched dynamics of density distributions for different λ subjected to anti-symmetric disorder, where the hopping strength suddenly changes from $t/J = 1$ to $t/J = 28$ at time $\tau = 50$. For the Hermitian case with $\lambda/J = 0$ [see Fig. S4(a1)], the initial localized mode remains mostly localized after the quench. The slight spreading of the density distribution is attributed to finite-size effects. As the asymmetric hopping parameter λ increases, the wavepacket initially localized at the center of the ladder becomes delocalized, and propagates towards the left boundary after the quench, and it is finally localized at the boundary, due to the interplay of the NHSE, inter-chain coupling and anti-symmetric disorder.

VI. ROBUSTNESS OF ANDERSON DELOCALIZATION AGAINST IMPERFECT ANTI-SYMMETRIC DISORDER

In the main text, we demonstrated that anti-symmetric disorder, defined by $\Delta_j^{(a)} = -\Delta_j^{(b)} = \Delta_j$, can give rise to Anderson delocalization in the coupled Hermitian and non-Hermitian chains. This Anderson delocalized phase allows the NHSE to reappear, even in the presence of ultra-strong disorder. In this section, we investigate how robust this phenomenon is when the anti-symmetric condition is no longer exact. To this end, we consider a modified disorder

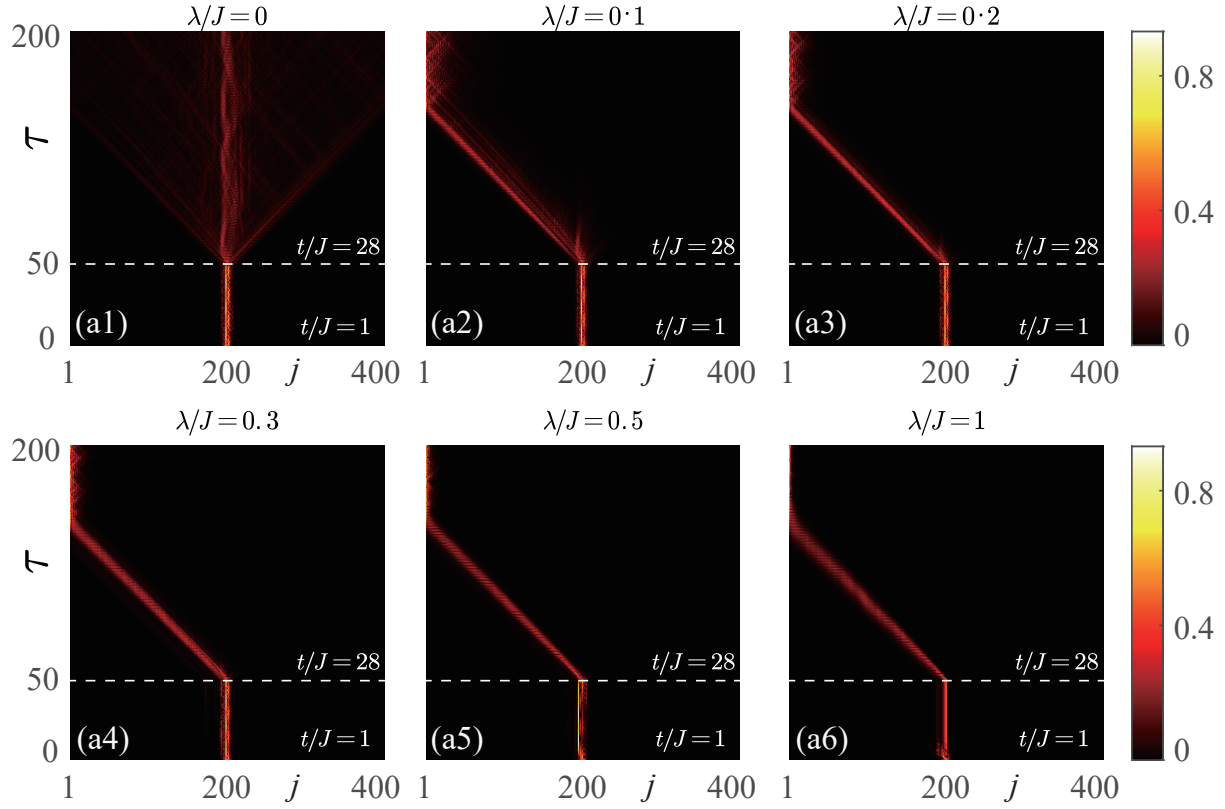

FIG. S4. Dynamical localization and delocalization via quench. Quenched dynamics of density distributions for different λ subjected to anti-symmetric disorder, where the initial state is set as the Gaussian wavepacket as $\psi_0(j) = \exp[-(j-j_0)^2/2\sigma^2]/\mathcal{N}$ centered at the site j_0 in the HN chain. At time $\tau = 50$, the hopping strength changes from $t/J = 1$ to $t/J = 28$. The parameters used are $\gamma/J = 1$, $W/J = 12$, and $N = 400$ with (a1) $\lambda/J = 0$, (a2) $\lambda/J = 0.1$, (a3) $\lambda/J = 0.2$, (a4) $\lambda/J = 0.3$, (a5) $\lambda/J = 0.5$, and (a6) $\lambda/J = 1$.

configuration where $\Delta_j^{(a)} = \Delta_j$ and $\Delta_j^{(b)} = -\Delta_j + \delta_j$, with δ_j being a random variable that quantifies deviations from perfectly anti-symmetry. Then, the Hamiltonian of the hybrid system reads

$$\begin{aligned}\hat{\mathcal{H}}_{\text{dis}} = &\sum_j \left[(\gamma+\lambda)\hat{a}_j^\dagger \hat{a}_{j+1} + (\gamma-\lambda)\hat{a}_{j+1}^\dagger \hat{a}_j\right] + \sum_j \left(J\hat{b}_{j+1}^\dagger \hat{b}_j + t\hat{a}_j^\dagger \hat{b}_j + \text{H.c.}\right) \\ &+ \sum_j \Delta_j \left(\hat{a}_j^\dagger \hat{a}_j - \hat{b}_j^\dagger \hat{b}_j\right) + \sum_j \delta_j \hat{b}_j^\dagger \hat{b}_j, \end{aligned} \tag{S10}$$

where Δ_j represents the anti-symmetric disorder applied to both the non-Hermitian and Hermitian chains. It is uniformly sampled from the interval $[-W/2,\ W/2]$, where W denotes the disorder strength. The term δ_j introduces a random perturbation that breaks the exact anti-symmetry, and is independently drawn from a uniform distribution in $[-\delta/2,\ \delta/2]$, with δ characterizing the degree of asymmetry in the disorder.

Figures S5(a) and (b) show the mcom and IPR, averaged over all eigenstates, in the presence of anti-symmetric disorder Δ_j and a random perturbation δ_j that explicitly breaks the anti-symmetry. These quantities are plotted as functions of the perturbation strength δ for $\lambda/J = 1$ in panel (a) and $\lambda/J = 1.5$ in panel (b), for two different values of the asymmetric hopping strength. In both cases, the finite value of the IPR indicates that the eigenstates of the coupled system remain localized, either due to Anderson localization or localization induced by the NHSE.

When the disorder deviates moderately from the anti-symmetric configuration, i.e., when the perturbation δ_j is of moderate strength, the eigenstates stay localized near the left boundary due to the re-emergent NHSE. The small value

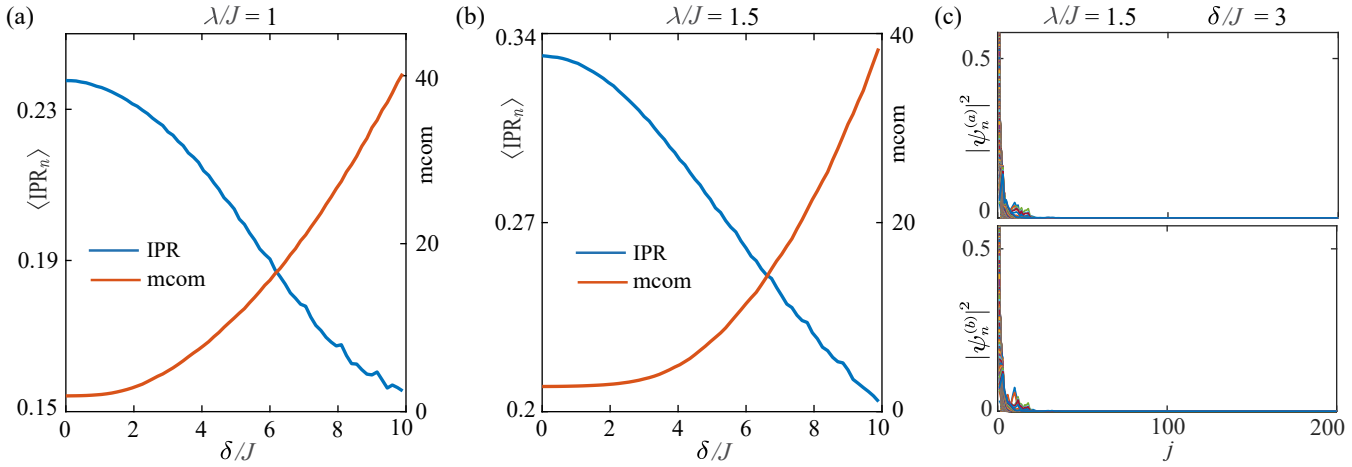

FIG. S5. Impact of imperfect anti-symmetric correlated disorder on Anderson delocalization. (a,b) IPR and mcom averaged over all the eigenstates, subject to anti-symmetric disorder Δ_j and a random perturbation δ_j that breaks the exact anti-symmetry, as a function of the perturbation strength δ for $\lambda/J = 1$ (a) and $\lambda/J = 1.5$ (b). The results are averaged over 2000 disorder realizations with $\gamma/J = 1$, $W/J = 12$, $t/J = 28$, and $N = 200$. (c) Probability density distributions $|\psi_n^{(a)}(j)|^2$ and $|\psi_n^{(b)}(j)|^2$ of all the eigenstates subject to anti-symmetric disorder Δ_j and a random perturbation δ_j for $\lambda/J = 1.5$ and $\delta/J = 3$ in one disorder realization with $N = 200$.

of mcom in Fig. S5(a) confirms the persistence of this re-emergent NHSE for deviations as large as approximately 16.7% at $\lambda/J = 1$, despite the presence of strong disorder Δ_j. Furthermore, for $\lambda/J = 1.5$, the NHSE persists even with a deviation of about 25% from the anti-symmetric disorder configuration, despite the presence of strong disorder, as shown in Fig. S5(b). For moderate values of δ, the eigenstates manifest as skin modes localized at the left boundary. As δ increases, a coexistence emerges between skin-mode localization and Anderson localization. With a further increase in δ, the system undergoes a transition into a regime dominated by strong perturbation-induced Anderson localization, where the eigenstates become localized in the bulk.

Figure S5(c) shows the probability density distributions $|\psi_n^{(a)}(j)|^2$ and $|\psi_n^{(b)}(j)|^2$ for all eigenstates, obtained from a single disorder realization with anti-symmetric disorder Δ_j and a random perturbation δ_j, with $\lambda/J = 1.5$ and $\delta/J = 3$. These distributions reveal the Anderson delocalization accompanied by the NHSE even with a deviation of 25% from the anti-symmetric disorder configuration.

These results demonstrate that the Anderson delocalization, accompanied by the re-emergent NHSE, remains robust even under strongly non-ideal anti-symmetric disorder, extending its applicability beyond fine-tuned scenarios.

VII. DEPENDENCE OF PHASE DIAGRAMS ON γ

In the main text, we plot the phase regions of Anderson localization and skin-mode localization as functions of W, γ and λ by fixing λ. Now, we consider the dependence of phase diagrams on γ under anti-symmetric disorder.

The phase diagrams determined by the winding number in the presence of anti-symmetric disorder are shown in Fig. S6(a–c), where the phase boundary between the absence ($w = 0$) and presence ($w = 1$) of skin modes is clearly visible. However, the winding number cannot identify the coexistence regions of skin-mode localization and Anderson localization. In contrast, this distinction can be made using the mcom, as shown in Fig. S6(d–f). Three distinct regions are observed: Anderson localization with mcom $\sim N/2$, skin-mode localization with mcom ~ 1, and a mixed phase characterized by $1 \ll \text{mcom} \ll N/2$. We find that the phase boundary becomes less sensitive to variations in γ once γ is sufficiently large. This results from the weakening of nonreciprocal hopping at large values of γ.

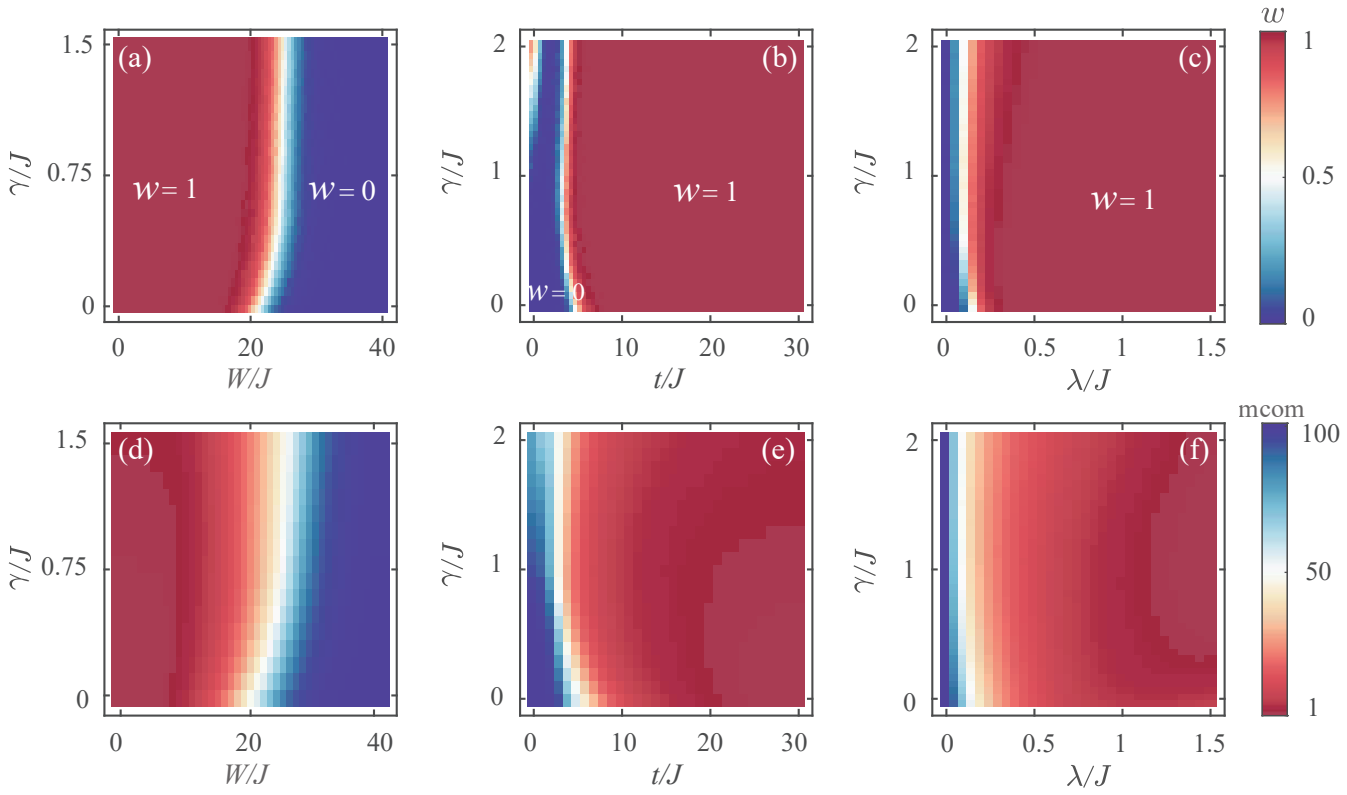

FIG. S6. (a-c) Winding number w and (d-f) mcom, under anti-symmetric disorder, in the (W, γ) plane with $\lambda/J = 1$ and $t/J = 14$ (a,d), the (t, γ) plane with $W/J = 12$ and $\lambda/J = 1$ (b,e), and the (λ, γ) plane with $W/J = 12$ and $t/J = 14$ (c,f). There exist three regions: Anderson localization with mcom $\sim N/2$, skin-mode localization with mcom ~ 1, and a mixture of the two with $1 \ll$ mcom $\ll N/2$, respectively. The results are averaged over 1200 disorder realizations with $N = 200$.

VIII. COEXISTENCE REGION OF ANDERSON AND SKIN-MODE LOCALIZATION

As shown in Fig. 3(d-f) of the main text, under strong disorder, the system exhibits Anderson localization for small inter-chain coupling t (region I). As the inter-chain coupling t increases, the system enters region III, where Anderson localization and skin-mode localization coexist. This is because increasing t effectively reduces the disorder strength, leading to competition between Anderson localization and the NHSE. With further increase in t, the system transitions into region II, where all eigenstates exhibit skin-mode localization due to the NHSE. In this region II, the effective disorder becomes quite weak at the large inter-chain coupling t for the anti-symmetric disorder configuration.

As explained in the main text, the winding number cannot identify the coexistence region (Region III), where both Anderson localization and skin-mode localization are present. Specifically, it cannot distinguish Region III from the pure skin-mode localization region (Region II). This limitation is expected, as the winding number reflects the presence of the NHSE. Even in the coexistence region, eigenstates under OBCs still exhibit skin-mode localization if their corresponding eigenvalues lie inside the point gap of the PBC spectrum, as illustrated in Fig. S7(a). Indeed, part of the OBC spectrum is enclosed by the point gap in the PBC spectrum. Eigenstates associated with eigenvalues inside this point gap are skin-mode localized [see Fig. S7(b)], whereas those outside the point gap are Anderson localized [see Fig. S7(c)]. Consequently, the winding number remains fixed at $W = 1$ throughout Region III, resulting in only two distinct regions being visible in the winding number phase diagram.

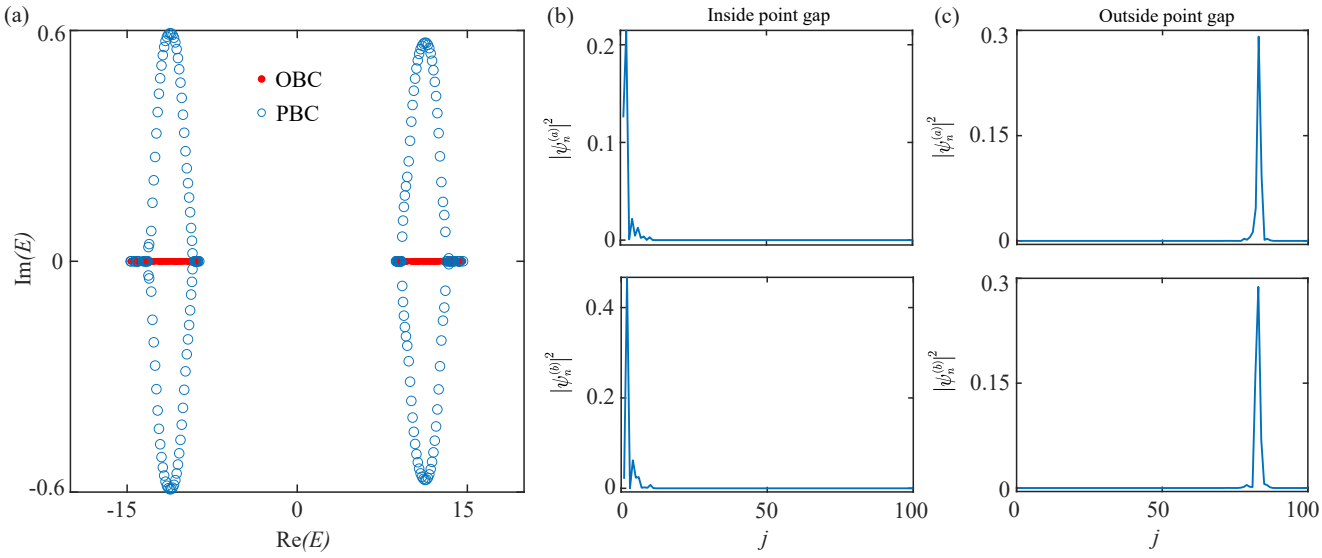

FIG. S7. (a) Complex eigenenergy spectra under OBCs (red dots) and PBCs (blue circles) in region III, where the Anderson localization and skin-mode localization coexist. (b,c) Probability density distributions $|\psi_n^{(a)}(j)|^2$ and $|\psi_n^{(b)}(j)|^2$ of specific eigenstates inside (b) and outside (c) the point gap. The parameters are $W/J = 20$, $t/J = 10$, and $\gamma/J = \lambda/J = 1$.

IX. CIRCUIT IMPLEMENTATION OF THE MODEL

In this section, we present a detailed circuit implementation of our model. Linear circuit networks, composed of linear components, can be characterized by a series of time-dependent differential equations. After applying the

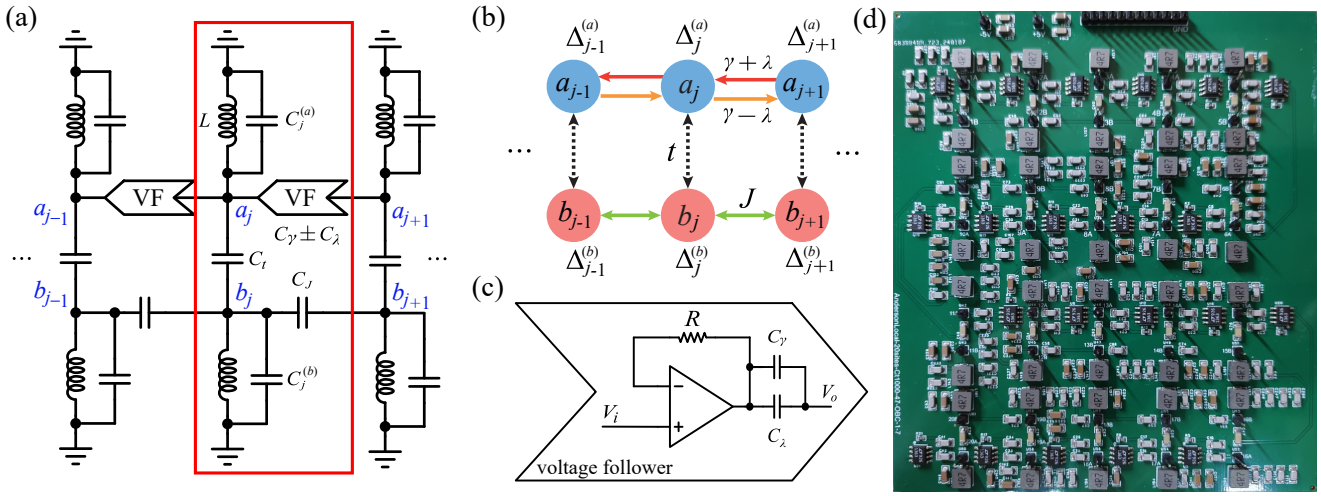

FIG. S8. Electrical-circuit lattice. (a) Circuit implementation of the coupled HN-Hermitian lattice subject to correlated disorder, corresponding to the tight-binding lattice model in (b). The red solid line outlines a unit cell, containing two sublattices a_j and b_j, in the circuit lattice. For the HN chain $\{a_j\}$, the nonreciprocal intra-chain hopping, represented by capacitors $C_\gamma \pm C_\lambda$, is realized by the voltage follower (VF). The circuit diagram of the voltage follower module is shown in (c), where the resistor $R = 1$ kΩ in the voltage follower is used to ensure its stability. The capacitor C_J denotes the intra-chain hopping in the Hermitian chain $\{b_j\}$, C_t represents the inter-chain hopping. $C_j^{(a)}$ and $C_j^{(b)}$ are disordered capacitances for simulating the correlated disorder. The inductor L is used to adjust the resonance frequency of the circuit. (d) Photograph of the whole printed circuit board.

Fourier transformation with respect to time, these equations can be simplified into a set of algebraic equations in the frequency domain. In the frequency domain, the relation of current and voltage between two nodes can be written as

$$I_{jk}(\omega) = \frac{V_j(\omega) - V_k(\omega)}{Z_{jk}(\omega)}, \tag{S11}$$

where $Z_{jk}(\omega)$ is the impedance between node j and node k, and the impedances of capacitor, inductor and resistor are $Z_C(\omega) = 1/i\omega C, Z_L(\omega) = i\omega L$ and $Z_R(\omega) = R$. According to Kirchhoff's current law, the sum of all currents entering and leaving a node equals zero. This indicates that the input current I_j at the node j equals the sum of the currents leaving node j:

$$I_j = \sum_k I_{jk}. \tag{S12}$$

According to Eqs. (S11) and (S12), we can derive the circuit Laplacian of the electrical circuit in Fig. S8(a), corresponding to the tight-binding lattice model in Fig. S8(b).

The equivalent circuit of the model is composed of inductors and capacitors. The voltage follower is used to equivalently simulate the non-reciprocal hopping of the model with $\gamma = \lambda$. The circuit diagram of the voltage follower module is shown in Fig. S8(c), where the resistor $R = 1$ kΩ in the voltage follower is used to ensure its stability. Capacitors are used to equivalently simulate the reciprocal hopping and onsite potential of the tight-binding model, where the capacitances of the capacitors C_γ, C_λ, C_t and C_J correspond to the reciprocal hopping strengths γ, λ, t and J in Fig. S8(b). The correlated disorders $\Delta_j^{(a)}$ and $\Delta_j^{(b)}$ are simulated by the disordered capacitances $C_j^{(a)}$ and $C_j^{(b)}$. In addition, the inductor L is used to adjust the resonance frequency of the circuit. The fabricated circuit boards are shown in Fig. S8(d).

The coupled HN-Hermitian chains in the main text can be represented by the Laplacian $J(\omega)$ of the circuit. The Laplacian is defined as the response of the voltage vector $\mathbf{V}$ to the input current vector $\mathbf{I}$ by

$$\mathbf{I}(\omega) = J(\omega)\mathbf{V}(\omega). \tag{S13}$$

According to Eq. (S11) and Eq. (S12), the Kirchhoff equation of the circuit in Fig. S8(a) is written as

$$\begin{aligned} I_{a,j} = \; & i\omega\left(C_\gamma + C_\lambda\right)\left(V_{a,j+1} - V_{a,j}\right) + i\omega\left(C_\gamma - C_\lambda\right)\left(V_{a,j-1} - V_{a,j}\right) + i\omega C_t\left(V_{b,j} - V_{a,j}\right) \\ & - i\omega\left(C_g + C_j^{(a)}\right)V_{a,j} - \frac{1}{i\omega L}V_{a,j}, \end{aligned} \tag{S14}$$

$$I_{b,j} = i\omega C_t\left(V_{a,j} - V_{b,j}\right) + i\omega C_J\left(V_{b,j+1} - V_{b,j}\right) + i\omega C_J\left(V_{b,j-1} - V_{b,j}\right) - i\omega\left(C_g + C_j^{(b)}\right)V_{b,j} - \frac{1}{i\omega L}V_{b,j}, \tag{S15}$$

where $I_{a,j}$ ($V_{a,j}$) and $I_{b,j}$ ($V_{b,j}$) denote the currents (voltages) on a and b sublattices in the jth cell, respectively, ω denotes the circuit frequency, and C_g is grounded capacitor for ensuring the circuit stability. In experiments, we take $C_\gamma = C_J$. Then, using Eqs. (S14) and (S15), the circuit Laplacian $J(\omega)$ is rewritten as

$$J(\omega) = i\omega\mathcal{H}_c - \left(2i\omega C_J + i\omega C_t + i\omega C_g + \frac{1}{i\omega L}\right)\mathbb{1}, \tag{S16}$$

where $\mathbb{1}$ is the $2N \times 2N$ identity matrix, and $\mathcal{H}_{\rm c}$ reads

$$\mathcal{H}_{\rm c} = \begin{pmatrix} -C_1^{(a)} & C_t & C_J + C_\lambda & 0 & \cdots & 0 & 0 \\ C_t & -C_1^{(b)} & 0 & C_J & \cdots & 0 & 0 \\ C_J - C_\lambda & 0 & -C_2^{(a)} & C_t & \cdots & 0 & 0 \\ 0 & C_J & C_t & -C_2^{(b)} & \cdots & 0 & 0 \\ \vdots & \vdots & \vdots & \vdots & \ddots & \vdots & \vdots \\ 0 & 0 & 0 & 0 & \cdots & -C_L^{(a)} & C_t \\ 0 & 0 & 0 & 0 & \cdots & C_t & -C_L^{(b)} \end{pmatrix}, \tag{S17}$$

The matrix $\mathcal{H}_{\rm c}$ in the first term of the circuit Laplacian $J(\omega)$ in Eq. (S16) replicates the Hamiltonian matrix of the coupled HN-Hermitian chains described in the main text. The second term of the circuit Laplacian $J(\omega)$ in Eq. (S16)

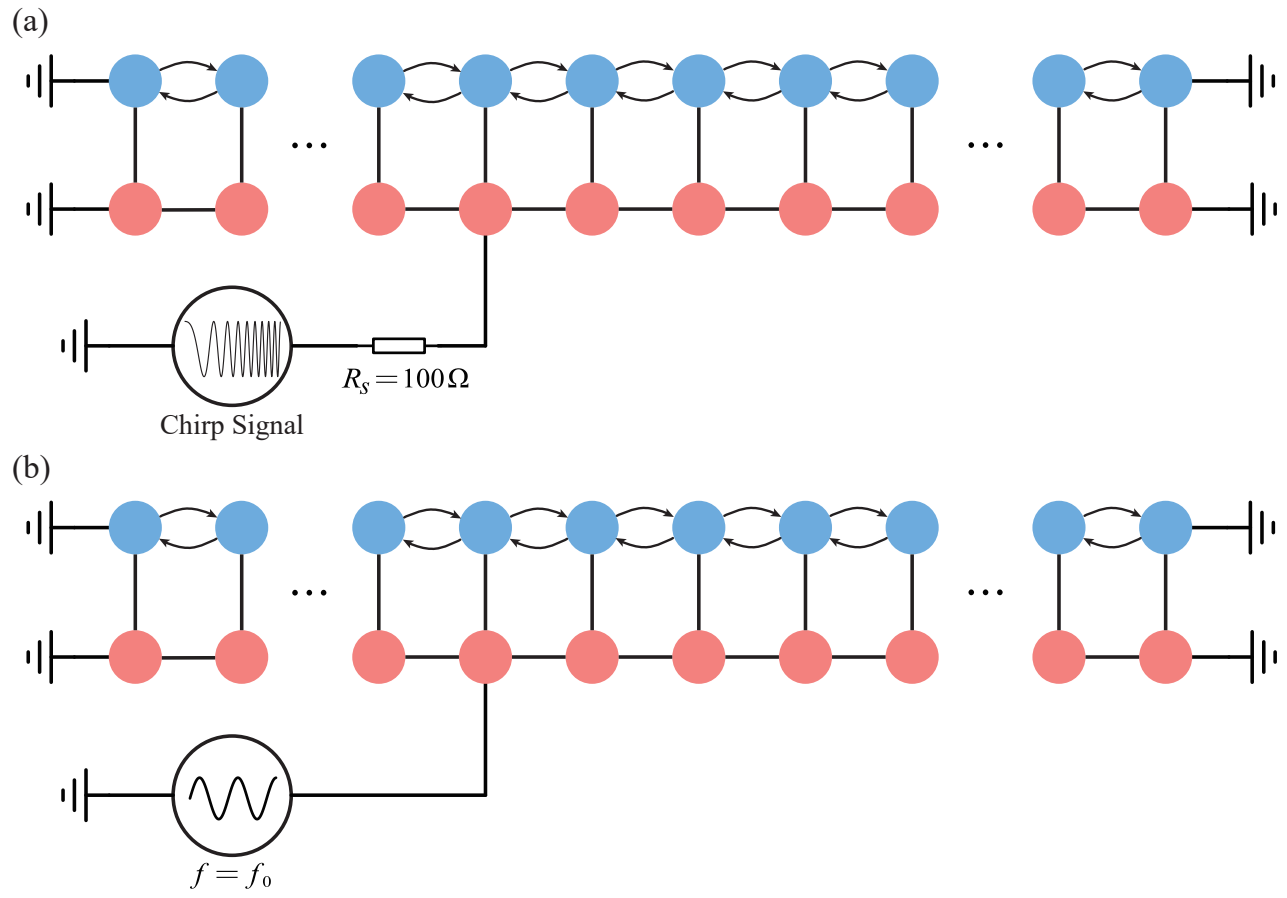

FIG. S9. Schematic of the experiment. (a) A chirp signal is used for analyzing the steady-state voltage response at different frequencies. (b) A monochromatic signal is used for measuring the temporal voltage response of the circuit under the specific frequency f_0.

does not influence the state localization and delocalization. Therefore, this allows the circuit Laplacian to model the desired Hamiltonian.

When the input current is zero, we can obtain the eigenvalue equation:

$$\mathcal{H}_{\mathrm{c}}\mathbf{V} = \left(2C_J + C_t + C_g - \frac{1}{\omega^2 L}\right)\mathbf{V}. \tag{S18}$$

This indicates that the voltage distribution reflects the state distribution corresponding to the specific eigenvalue by adjusting the frequency $f = \omega/(2\pi)$ of the excited voltage. By measuring the voltage response of the excitation, we can experimentally verify the state delocalization and localization of the coupled HN-Hermitian chains subject to the correlated disorder.

A printed circuit board (PCB) layout is simulated using LTSpice, designed and manufactured using LCEDA. The non-reciprocal hopping is implemented using voltage followers based on the unity-gain stable operational amplifier model LT1363. In the circuit, 1 kΩ (±1% tolerance) resistors are employed to maintain the stability of the operational amplifier, and 100 nF (±10% tolerance) and 2.2 μF (±10% tolerance) capacitors are used to suppress ripple noise from the direct current (DC) power supply.

To measure eigenstates, a signal generator (Keysight 33500B) is used to generate a chirp signal, which is then injected into the circuit. The voltage response to this signal is recorded using an oscilloscope (Keysight DSOX4024A) to diagnose the resonance frequency f. With this frequency f, the circuit is excited at a certain node, and the voltage response is measured on all nodes to obtain the eigenstates. For temporal measurements, the signal generator is utilized to produce a sinusoidal signal with frequency f and duration of 150 μs, and this signal is injected to a certain node of the circuit. The oscilloscope then measures the voltage response at all the nodes to obtain the time-evolving states.

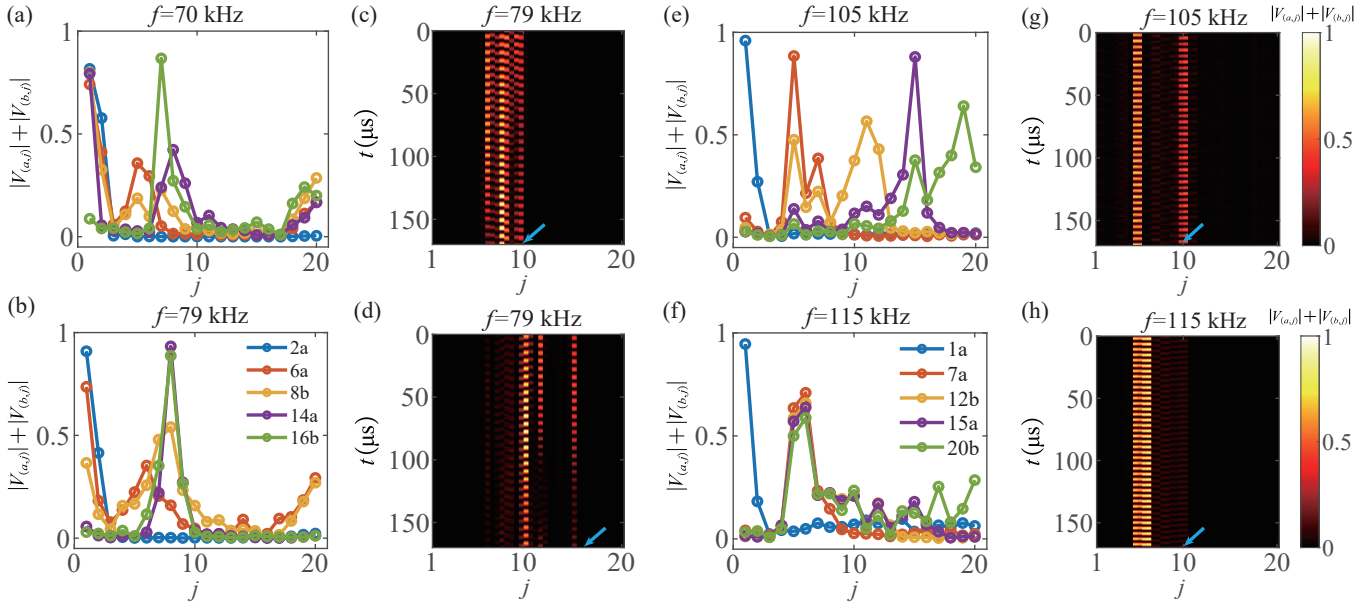

FIG. S10. Experimental observations of the Anderson localization of HN-Hermitian coupled chains subject to symmetric disorder. (a,b) Measured site-resolved voltage distributions $|V_{a,j}| + |V_{b,j}|$ (j is unit-cell index) at resonance frequencies $f =$ 70 kHz (a) and $f =$ 79 kHz (b) for weak inter-chain hopping C_t, with $C_\gamma = C_\lambda = C_J = C_t =$ 100 nF, $L =$ 4.7 μH, and $C_j^{(a)} = C_j^{(b)} \in [-6C_J,\ 6C_J]$. The legend "$j\alpha$" ($\alpha = a, b$) in (b) indicates the excitation at the jth site of the chain α. (c,d) Measured temporal voltage responses excited at the 11th (c) and 17th (d) unit cells, indicated by the blue arrows, for the weak inter-chain hopping with $f =$ 79 kHz. (e,f) Measured voltage distributions and (g,h) temporal voltage responses for strong inter-chain hopping C_t, with $C_\gamma = C_\lambda = C_J =$ 47 nF, $C_t =$ 1 μF, $L =$ 4.7 μH, and $C_j^{(a)} = C_j^{(b)} \in [-6C_J,\ 6C_J]$.

In experiments, we excite the circuit at a certain node, and then test the voltage response at all nodes. The schematic of the testing is shown in Fig. S9. A chirp signal (10 kHz - 400 kHz) is used for analyzing the steady-state voltage response at different frequencies [see Fig. S9(a)]. A monochromatic signal, e.g. sinusoidal wave, is used for measuring the temporal voltage response of the circuit under the specific frequency [see Fig. S9(b)].

X. EXPERIMENTAL RESULTS OF HN-HERMITIAN COUPLED CHAINS SUBJECT TO THE SYMMETRIC DISORDER

As shown in the main text, the experimental results have proved that the strong inter-chain coupling can lead to the re-emergent NHSE in the coupled NH-Hermitian chains in spite of the strong anti-symmetric disorder. In this section, as a comparison, we present experimental results of the coupled HN-Hermitian chains subject to symmetrically-correlated disorder. We resonantly excite the circuit, and measured the site-resolved voltage distributions $|V_{a,j}|+|V_{b,j}|$ in the presence of symmetric disorder. As shown in Fig. S10(a,b) for weak inter-chain coupling and Fig. S10(e,f) for strong inter-chain coupling, the voltage distributions remain mostly localized. Furthermore, we measure the temporal voltage response, as shown in Fig. S10(c,d) for weak inter-chain coupling and Fig. S10(g,h) for strong inter-chain coupling. Once it is excited, the voltage remains localized as time evolves.

---

* These authors contributed equally
† E-mail: wjuphy@scut.edu.cn
‡ E-mail: yangzm@scut.edu.cn
§ E-mail: liutao0716@scut.edu.cn

[1] M. Creutz, "End states, ladder compounds, and domain-wall fermions," Phys. Rev. Lett. 83, 2636 (1999).
[2] E. Abrahams, P. W. Anderson, D. C. Licciardello, and T. V. Ramakrishnan, "Scaling theory of localization: Absence of quantum diffusion in two dimensions," Phys. Rev. Lett. 42, 673 (1979).
[3] N. Hatano and D. R. Nelson, "Localization transitions in non-Hermitian quantum mechanics," Phys. Rev. Lett. 77, 570 (1996).
[4] Z. Gong, Y. Ashida, K. Kawabata, K. Takasan, S. Higashikawa, and M. Ueda, "Topological phases of non-Hermitian systems," Phys. Rev. X 8, 031079 (2018).
[5] Y.-X. Xiao and C. T. Chan, "Topology in non-Hermitian Chern insulators with skin effect," Phys. Rev. B 105, 075128 (2022).